

Dynamic Stability Analysis of a Hybrid Wave and Photovoltaic Power Generation System Integrated into a Distribution Power Grid

Li Wang, *Senior Member, IEEE*, Quang-Son Vo, and Anton V. Prokhorov, *Member, IEEE*

Abstract--This paper evaluates the dynamic stability of a hybrid wave and photovoltaic (PV) power generation system integrated into a distribution power grid. The wave power-generation system (WPGS) is simulated by a linear permanent-magnet generator (LPMG) driven by an Archimedes wave swing (AWS). The outputs of the WPGS and the PV system are connected to a common dc link through a voltage-source converter (VSC) and a dc/dc boost converter, respectively. The common dc link is interfaced to the distribution power grid via a voltage-source inverter (VSI). A supercapacitor (SC) is utilized to smooth the generated power delivered to the distribution power grid. This paper proposes a control scheme to maintain stable operation of the studied system while achieving maximum power extractions for the wave system and the PV system. Both root-loci analysis of the system eigenvalues under various operating conditions and the time-domain simulation results of the studied system subject to disturbance conditions are presented to demonstrate and verify the effectiveness of the SC combined with the proposed control scheme on performance improvement of the studied hybrid wave and PV system.

Index Terms--Distribution power grid, dynamic stability, linear permanent-magnet generator, photovoltaic array, root-loci analysis, supercapacitor, time-domain simulations.

I. INTRODUCTION

DUE to the rapid depletion of fossil fuel reserves and the environmental issues, renewable energy has increasingly attracted worldwide attention over the past few decades. While the large-scale renewable-energy power-generation systems are integrated into the bulk power transmission networks [1], the increasing utilization of the small-scale renewable energy sources (RESs) in the distributed generation systems is also the current trend [2], [3]. To increase the system reliability, cost-effective, and/or system efficiency, etc., two or more RESs can be combined together or with the conventional non-renewable energy sources such as fossil fuel forming the hybrid power-generation systems (HPGSs) [4]–[6]. Due to the fluctuating and intermittent nature of the RESs, the energy

storages such as battery, supercapacitor (SC), superconducting magnetic energy storage (SMES), hydrogen, etc., are usually required in the HPGSs for power back-up to manage and/or smooth the fluctuated power. Such HPGSs can operate in standalone mode to supply the isolated loads or in grid-connected mode [5].

Various topics related to the HPGSs have been extensively reported in literature [2], [6]–[16]. The authors in [2] presented the dynamic modeling and control of a proposed grid-connected PV-wind-battery HPGS with versatile power transfer which enabled the multi-modes of operation of the proposed system. In [6], a HPGS combining wind, PV, FC, electrolyzer, and battery was proposed for the stand-alone applications while a power management strategy was designed for the system to coordinate the power flows among the different energy sources. Several power management strategies of the grid-connected HPGSs were proposed in [7]–[9]. A design optimization of an autonomous wind-PV-battery HPGS was illustrated in [10] whereas a design optimization technique for a grid-connected wind-PV-battery HPGS based on a multi-objective genetic algorithm was reported in [11]. Dynamic stability of a microgrid connecting with a wind turbine generator, a diesel synchronous generator, and a battery-based energy storage system was investigated in [12] while the small-signal stability improvement results of a grid-connected PV-diesel engine HPGS using an auxiliary signal in PV control loop were presented in [13]. The authors in [14] proposed a novel control scheme based on the state of charge of the battery to improve the performance of a wind-PV-battery-based HPGS. The application of a SMES to enhance dynamic security of a grid-connected wind-PV HPGS during grid voltage sag was investigated in [15] while the voltage stabilization of a hybrid microgrid using SCs was reported in [16].

It should be noted that most of the proposed HPGSs reported in literature were mainly based on wind and PV. This is due to the fact that wind and PV can complement each other and their technologies have been well-established. Nevertheless, ocean energy which is an abundant RES has been steadily developing towards pre-commercial and commercial operation in recent years [17]. This is likely that the ocean energy will contribute a significant portion to the electricity generation portfolio in the very near future. Among the available forms of ocean energy such as wave, marine

L. Wang is with the Department of Electrical Engineering, National Cheng Kung University, Tainan City 70101, Taiwan (e-mail: liwang@mail.ncku.edu.tw).

Q.-S. Vo is with the Department of Electrical Engineering, National Cheng Kung University, Tainan City 70101, Taiwan (e-mail: vqson80@gmail.com).

A. V. Prokhorov is with the Institute of Power Engineering, Tomsk Polytechnic University, Tomsk 634050, Russia (e-mail: antonprokhorov@tpu.ru).

current, tidal, ocean thermal, etc., wave energy is one of the most interesting and promising sources for electricity generation due to its features of high power density and widespread availability [18]-[21].

Although a great deal of excellent research on the topics of wave power-generation systems (WPGSs) has been undertaken and reported [17]-[29], the combination of the WPGSs with other RESs in the HPGSs has not been widely studied. Only a few published papers such as [30]-[32] have reported about the HPGSs including the wave power. The integration of wind and wave power generation systems using a dc microgrid was studied and reported in [30] while a combination of four different wave energy conversion devices connected to a distribution substation was represented in [31]. The authors in [32] had developed a standalone PV-wave hybrid renewable power generation system for implementing in island areas in Malaysia. In that hybrid scheme, the WPGS was simulated by a PMSG driven by an oscillating water column device and the battery bank was used as a backup energy-storage system.

In this paper, the dynamic stability analyzed results of a grid-connected wave and PV HPGS with the support of the SC for smoothing out the power fluctuations are presented. A control scheme is proposed to smooth power fed to the grid and maintain the stable operation of the studied system while extracting maximum power from both wave and PV renewable resources. The performance of the studied system and the effectiveness of the SC combined with the proposed control scheme are examined through both the root-loci analysis results of the system eigenvalues and the time-domain simulation results.

This paper is organized as follows. The configuration and employed mathematical models of the studied system are presented in Section II. The control scheme for the studied system is discussed in Section III. The root-loci of system eigenvalues and the time-domain simulation results of the system are depicted in Sections IV and V, respectively. Finally, main conclusions of this paper are drawn in Section VI.

II. SYSTEM CONFIGURATION AND MATHEMATICAL MODELS

A. Configuration of the Studied System

Fig. 1 shows the configuration of the studied hybrid wave and PV system connected to a distribution power grid. The PV system and the wave power-generation system (WPGS) are integrated to a common dc link through a dc/dc boost converter and an ac/dc voltage-source converter (VSC), respectively. The common dc link is interfaced with the distribution power grid via a dc/ac voltage-source inverter (VSI). The dc/dc boost converter connecting the PV array to the common dc link has a maximum power point tracking (MPPT) function to make it operate as an MPPT controller. The WPGS consists of a linear permanent-magnet generator (LPMG) driven by an Archimedes wave swing (AWS). The detailed configuration and operating principle of the AWS-based WPGS can be referred to [22]-[24], [29].

Since the powers supplied to the dc link from the WPGS

and the PV array are fluctuated, an energy storage device can be utilized to support for smoothing these power fluctuations. Generally, batteries have been widely used with the renewable power generation systems due to their advantages in terms of low capital cost, high energy density, and mature technology [33]-[35]. However, the batteries have several drawbacks such as low power density, slow response time, limited number of cycles, and short lifespan [34], [35] which make them become less desirable to be used for compensating the fast power fluctuations, particularly the ones with high value of peak-to-average power ratio produced by the WPGS. In order to perform the function of compensating the fast power fluctuations with high value of peak-to-average power ratio of the WPGS and the high-frequency power fluctuations of the PV array, the employed energy storage device should have the characteristics of high power density and fast response time during charging and discharging stages. In addition, the employed energy storage device is also desired to have large number of cycles, long lifespan, high efficiency, and low maintenance cost. The emerging energy storage technologies such as supercapacitor (SC) and superconducting magnetic energy storage (SMES) can be the good candidates for satisfying the aforementioned requirements [35]-[37]. The SC and the SMES could compete with each other since they have similar merits in terms of high power density, fast response time, and long service life. The advantage of the SC over the SMES is that it does not require any cooling system whereas the SMES must be operated in conjunction with a cryogenic refrigerator and related subsystems. Therefore, the SC is adapted for smoothing the power fluctuations of the studied hybrid wave and PV power generation system in this paper. The SC is also connected to the dc link through a bidirectional dc/dc converter.

To smooth the power fluctuations and maintain stable operation of the studied system while achieving the maximum power extractions from the renewable-energy sources, the control functions of the converters and the inverter must be properly performed. The control scheme for the studied system will be discussed in the next section. The employed mathematical models for each subsystem shown in Fig. 1 are described hereafter.

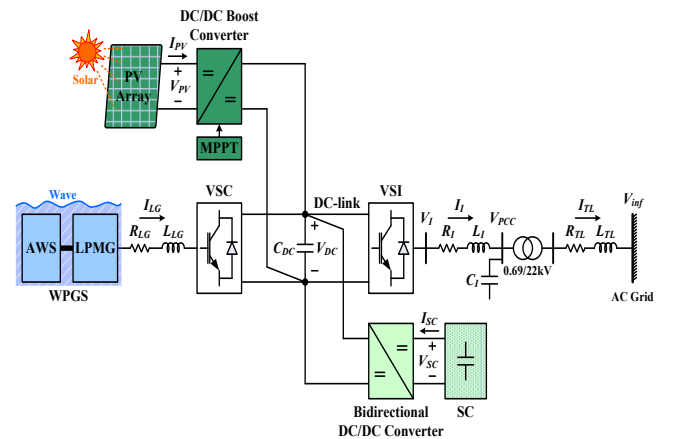


Fig. 1. Configuration of the studied hybrid wave and PV system integrated into a distribution power grid.

B. Model of AWS-Based WPGS

The model of the AWS-based WPGS describes the mechanical dynamics of the AWS and the electrical dynamics of the LPMG. Since the floater of the AWS is directly coupled with the translator of the LPMG, they can be combined as a single mass. The mass-spring-damper system [24] can be used to model the dynamics of the AWS. Thus, the mechanical dynamics of the AWS can be described by the motion equation as follows [18], [23], [29]:

$$\begin{aligned} p(z) &= u_z & (1) \\ (m_i)p(u_z) &= F_{\text{wave}} - K_S z - K_D u_z - F_{LG} & (2) \end{aligned}$$

where p is the differential operator with respect to time t ($p = d/dt$); z and u_z are the distance and speed of the floater, respectively; m_i is the total mass of the floater and the LPMG translator; F_{wave} is the driving force acting on the floater from the waves, F_{LG} is the force acting on the floater from the LPMG; and K_D and K_S are the damping coefficient and spring constant of the AWS, respectively.

The LPMG's model based on dq -axis reference frame fixed in the translator can be written by [18], [23], [29]:

$$(L_{dLG})p(i_{dLG}) = \omega_z L_{qLG} i_{qLG} - R_{LG} i_{dLG} - v_{dLG} \quad (3)$$

$$(L_{qLG})p(i_{qLG}) = \omega_z \psi_{PM} - \omega_z L_{dLG} i_{dLG} - R_{LG} i_{qLG} - v_{qLG} \quad (4)$$

where i_{dLG} and i_{qLG} (v_{dLG} and v_{qLG}) are the d - and q -axis currents (voltages), respectively; R_{LG} is the stator-winding resistance, L_{dLG} and L_{qLG} are the d - and q -axis synchronous inductances, respectively; ψ_{PM} is the flux linkage of the permanent magnet; and $\omega_z = \pi u_z / \tau_p$ (τ_p is the pole pitch) of the LPMG.

C. Model of PV Array and dc/dc Boost Converter

The PV array is composed of several PV modules interconnected in series and/or in parallel. Each PV module is constituted by a number of PV cells connected in series. Fig. 2 shows the single-diode equivalent-circuit model of a PV cell [38]-[42] which consists of a current source I_{ph} , a diode D_j , a parallel resistance R_p , and a series resistance R_s . By extending the model of a PV cell to represent a PV array as presented in [40], [41], the output current (in A) of the studied PV array can be expressed by

$$\begin{aligned} I_{PV} &= N_{mp} I_{ph} - N_{mp} I_0 \left\{ \exp \left[\frac{q(V_{PV} + R_{sa} I_{PV})}{kATN_s N_{ms}} \right] - 1 \right\} \\ &\quad - (V_{PV} + R_{sa} I_{PV}) / R_{pa} \end{aligned} \quad (5)$$

where V_{PV} is the output voltage (in V) of the PV array; N_{ms} and N_{mp} are the numbers of PV modules connected in series and in parallel, respectively; N_s is the number of the series-connected cells in a PV module; R_{sa} and R_{pa} are the equivalent series and parallel resistances (in Ω) of the PV array, respectively; and I_{ph} and I_0 are the photovoltaic and reverse saturation currents (in A), respectively. The currents I_{ph} and I_0 are given as follows [38]-[42]:

$$I_{ph} = [I_{sc,n} + \kappa_i (T - T_n)] \cdot (G / G_n) \quad (6)$$

$$I_0 = I_{0,n} (T / T_n)^3 \exp \left[(qE_g / kA) (1/T_n - 1/T) \right] \quad (7)$$

in which

$$I_{0,n} = I_{sc,n} / \left\{ \exp \left[(qV_{oc,n}) / (kAT_n N_s) \right] - 1 \right\} \quad (8)$$

where T and G are the operating temperature (in K) and solar irradiance (in W/m^2), respectively; $I_{sc,n}$ and $V_{oc,n}$ are the short-circuit current (in A) and open-circuit voltage (in V) in the standard test condition of $T_n = 298.15$ K (25 °C) and $G_n = 1000$ W/m^2 ; $I_{0,n}$ is the reverse saturation current at T_n ; κ_i is the short-circuit current coefficient (in A/K); E_g is the band gap energy of the semiconductor (in eV); q , k , and A are the electron's charge (in C), Boltzmann constant (in J/K), and diode ideality factor, respectively.

Fig. 3(a) plots the schematic diagram of the studied dc/dc boost converter for connecting the PV array to the dc link. Assume that the detailed switching actions of the switch S and the diode D shown in Fig. 3(a) are neglected. The dc/dc boost converter can be represented by the dynamic average-value model as shown in Fig. 3(b). Thus, the dynamic equations used to simulate the dc/dc boost converter can be obtained by [43], [44]:

$$(C_P)p(V_{PV}) = i_{PV} - i_{LP} \quad (9)$$

$$(L_P)p(i_{LP}) = -R_P i_{LP} + V_{PV} - (1 - D_P)V_{DC} \quad (10)$$

$$i_{PV_DC} = (1 - D_P)i_{LP} \quad (11)$$

where C_P is the capacitance of the input filter; L_P and R_P are the inductance and parasitic resistance of the energy-storage inductor of the converter, respectively; i_{LP} is the inductor current; i_{PV_DC} is the current fed to the dc link from the boost converter; V_{DC} is the dc-link voltage; and D_P is the duty ratio of the dc/dc boost converter.

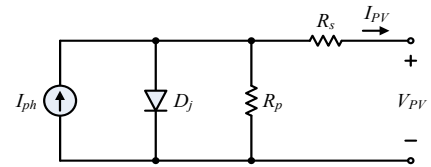


Fig. 2. Single-diode equivalent-circuit model of a PV cell.

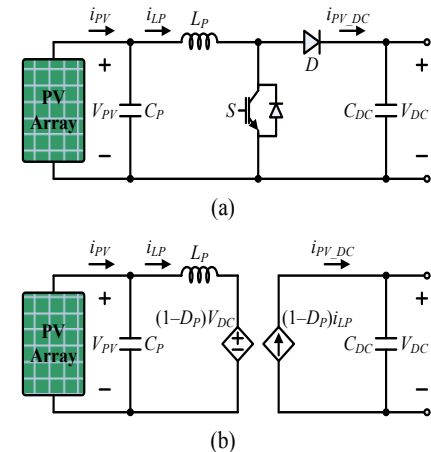


Fig. 3. Schematic diagram and dynamic average-value model of the dc/dc boost converter. (a) Schematic diagram. (b) Dynamic average-value model.

D. Model of SC and dc/dc Bidirectional Converter

Fig. 4 illustrates the equivalent-circuit model of the studied SC [45]. In addition to the capacitance C_{SC} of the SC, this model also takes into account the Joule loss and self-discharge phenomenon of the SC, which are represented by the resistances R_{SSC} and R_{pSC} , respectively. Based on Fig. 4, the corresponding dynamic equations of the employed SC can be obtained as [46]:

$$(C_{SC})p(V_{SC}) = -i_{SC} - V_{SC}/R_{pSC} \quad (12)$$

$$V_{SC} = V_{CSC} - R_{SSC}i_{SC} \quad (13)$$

where V_{SC} and i_{SC} are the voltage and current of the SC, respectively; and V_{CSC} is the voltage across C_{SC} .

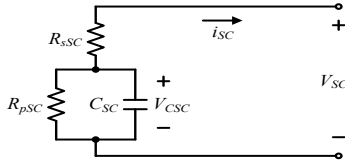


Fig. 4. Equivalent-circuit model of the SC.

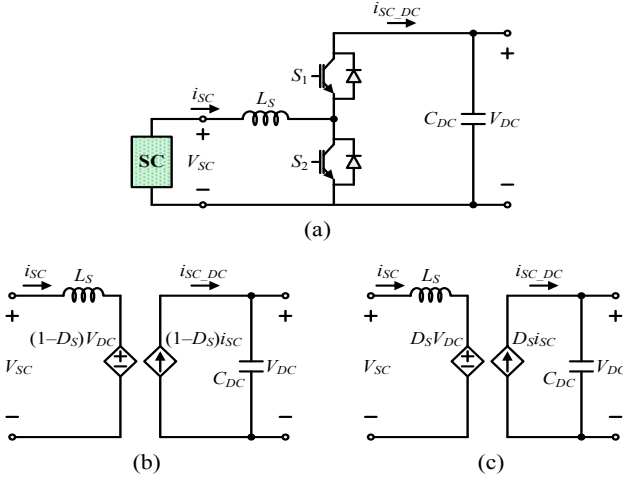


Fig. 5. Schematic diagram and dynamic average-value model of the bidirectional dc/dc converter. (a) Schematic diagram, (b) Dynamic average-value model of boost mode. (c) Dynamic average-value model of buck mode.

Fig. 5(a) shows the schematic diagram of the employed bidirectional dc/dc converter for interfacing the SC to the dc link. The low-voltage side of the bidirectional dc/dc converter is connected to the SC while its high-voltage side is tied to the dc link. The converter consists of an energy-storage inductor L_S and two switches S_1 and S_2 which are operated in a complementary manner. This configuration enables the feature of the bidirectional power flow of the converter. In buck mode of operation, the switch S_1 acts as a switch and S_2 acts as a diode [47], and the power flows from the dc link to the SC. Conversely, in boost mode of operation, the switch S_2 acts as a switch while S_1 acts as a diode, and the power flows from the SC to the dc link. Similarly, when modeling the dc/dc boost converter in the previous subsection, the detailed switching manners of the switches are neglected. Thus, the bidirectional dc/dc converter can be simulated by using its dynamic average-value model. Figs. 5(b) and 5(c) plot the dynamic

average-value model of the bidirectional dc/dc converter under boost mode and buck mode of operation, respectively. The dynamic equations for these two modes of operation are given below.

a) Boost mode:

$$(L_S)p(i_{SC}) = -R_S i_{SC} + V_{SC} - (1-D_S)V_{DC} \quad (14)$$

$$i_{SC_DC} = (1-D_S)i_{SC} \quad (15)$$

b) Buck mode:

$$(L_S)p(i_{SC}) = -R_S i_{SC} + V_{SC} - D_S V_{DC} \quad (16)$$

$$i_{SC_DC} = D_S i_{SC} \quad (17)$$

where L_S and R_S are the inductance and parasitic resistance of the energy-storage inductor, respectively; i_{SC_DC} is the current at the dc-link side; and D_S is the duty ratio of the bidirectional dc/dc converter.

E. Model of Voltage-source Inverter

The VSI, as shown in Fig. 1, is connected to the distribution power grid through an LC filter, a step-up transformer, and a connection line. The dynamic models of these components under dq -axis reference frame can be written as

$$(L_l)p(i_{dl}) = -R_l i_{dl} + \omega_e L_l i_{ql} + v_{dl} - v_{dPCC} \quad (18)$$

$$(L_l)p(i_{ql}) = -R_l i_{ql} - \omega_e L_l i_{dl} + v_{ql} - v_{qPCC} \quad (19)$$

$$(C_l)p(v_{dPCC}) = i_{dl} - i_{dTL} + \omega_e C_l v_{qPCC} \quad (20)$$

$$(C_l)p(v_{qPCC}) = i_{ql} - i_{qTL} - \omega_e C_l v_{dPCC} \quad (21)$$

$$(L_{TL})p(i_{dTL}) = -R_{TL} i_{dTL} + \omega_e L_{TL} i_{qTL} + v_{dPCC} - v_{dinf} \quad (22)$$

$$(L_{TL})p(i_{qTL}) = -R_{TL} i_{qTL} - \omega_e L_{TL} i_{dTL} + v_{qPCC} - v_{qinf} \quad (23)$$

where $(v_{dl}$ and $v_{ql})$ and $(i_{dl}$ and $i_{ql})$ are the output voltages and currents of the VSI; $(v_{dPCC}$ and $v_{qPCC})$ and $(v_{dinf}$ and $v_{qinf})$ are the voltages of the point of common coupling (PCC) and the distribution power grid, respectively; $(i_{dTL}$ and $i_{qTL})$ are the currents of the connection line; and ω_e is the electrical angular frequency (in rad/s).

III. CONTROL STRATEGY

The control strategy of the studied system is discussed in this section. The objectives of the control strategy are to smooth the power fed to the distribution power grid and maintain stable operation of the system under different operating conditions while extracting the maximum power available from the two renewable-energy sources. The maximum power extractions of the PV array and the WPGS can be achieved by properly performing the control functions of the dc/dc boost converter and the VSC, respectively. To supply the distribution power grid with the smoothed power and maintain stable voltage of the dc link, which is the key importance for the operation of the studied converters and the inverter, the control functions of the VSI and the bidirectional dc/dc converter need to be effectively coordinated with each other. The power fed to the distribution power grid is controlled by the controller of the VSI while the voltage of the

dc link is maintained by the controller of the bidirectional dc/dc converter. The detailed control strategies of the converters and the VSI are presented in the following subsections.

A. Control of dc/dc Boost Converter for PV Array

The generated output power of the PV array not only varies with the varying solar irradiance and ambient temperature but also depends on the terminal voltage of the PV array. For efficient operation of the PV array, its maximum power point (MPP) needs to be tracked continuously. To accomplish this goal, the dc/dc boost converter that connects the PV array to the dc link can be controlled to regulate the terminal voltage of the PV array to the desired value that corresponds to the MPP.

There have been several MPPT algorithms proposed in literature for implementing with the dc/dc converters used in the PV systems such as the perturb and observe (P&O), the incremental conductance (IC), and the constant voltage (CV). In this paper, the widely used P&O MPPT algorithm is employed for controlling the dc/dc boost converter. The detailed principle and the flowchart of the P&O MPPT algorithm can be referred to [7], [38].

B. Control of VSC for WPGS

Fig. 6 shows the control block diagram of the VSC. The controller of the VSC is adapted in the dq -axis reference frame fixed to the translator of the LPMG. The objectives of this controller are to enable the WPGS to capture maximum power from the wave and to minimize the power loss in the LPMG. As presented in [23], the power loss in the LPMG and the active power converted from the wave can be independently controlled by the d - and q -axis currents of the LPMG (i_{dLG} and i_{qLG}), respectively. The current control scheme of the VSC, as shown in Fig. 6, uses the proportional-integral (PI) controllers to regulate the d - and q -axis currents of the LPMG to the reference values (i_{dLG_ref} and i_{qLG_ref}). The reference value of the d -axis current is set equal to zero, i.e. $i_{dLG_ref} = 0$, for minimizing the power loss in the LPMG. In order for WPGS to capture maximum power from the wave, the reference value of the q -axis current is determined from the measured speed of the floater of the AWS as follows [23]:

$$i_{qLG_ref} = (2\tau K_D u_z) / (3\pi\psi_{PM}) \quad (24)$$

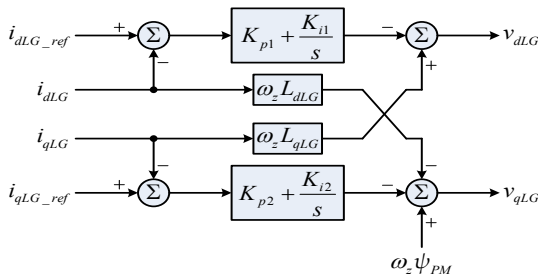


Fig. 6. Control block diagram of the employed VSC of WPGS.

C. Control of VSI for Distribution Power Grid

Fig. 7 depicts the control block diagram of the VSI. The controller of the VSI is used to control the active power

transferred through the VSI and to maintain the voltage magnitude of the PCC at the reference value. In order to acquire the decoupled control of the active and reactive components, the control of the VSI is performed in the dq -axis reference frame with the d -axis aligned with voltage vector of the PCC. Thus, the active power transferred through the VSI and the voltage of the PCC are controlled via the d - and q -axis currents of the VSI (i_{dI} and i_{qI}), respectively. The controller of the VSI, as shown in Fig. 7, has the cascaded structure in which the outer control loops regulate the active power transferred through the VSI and the voltage at the PCC while the inner control loops regulate the d - and q -axis currents of the VSI.

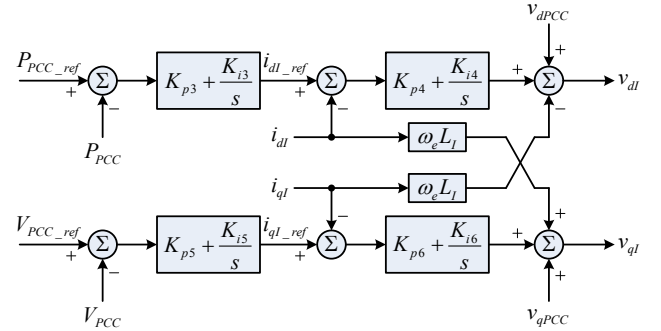


Fig. 7. Control block diagram of the VSI.

In order for the VSI can effectively transfer all the generated powers of the WPGS and the PV array to the distribution power grid and smooth out the power fluctuations, the reference value of the active power transferred through the VSI (P_{PCC_ref}) can be specified equal to the sum of the average powers of the WPGS and PV array. This can be accomplished by employing the averaging mechanism as illustrated in Fig. 8. The generated powers of the WPGS (P_{LG}) and the PV array (P_{PV}) are passed through the low-pass filters (LPFs) for averaging. The sum of the filtered signals is used as P_{PCC_ref} . In Fig. 8, T_1 and T_2 are the time constants of the LPFs. Different values of T_1 and T_2 will result in different averaging effects. To smooth out the power fluctuations due to the wave, T_1 can be chosen equal to the wave period T_{wave} . The time constant T_2 can be properly selected to smooth out the high-frequency power fluctuations in the generated power of the PV array.

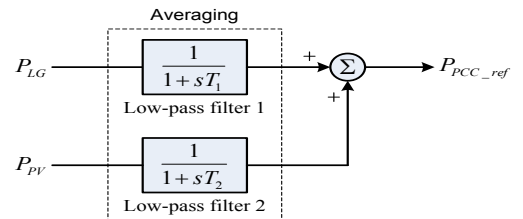


Fig. 8. Determination of the reference value (P_{PCC_ref}) for the active power control loop of the VSI.

D. Control of Bidirectional dc/dc Converter for SC

Fig. 9 plots the control block diagram of the bidirectional dc/dc converter that connects the SC to the dc link. The controller of the bidirectional dc/dc converter is based on two

cascaded feedback control loops. The outer control loop maintains the dc-link voltage V_{DC} at its reference value V_{DC_ref} and the inner control loop regulates the current of the SC i_{SC} . When the dc-link voltage departs from its reference value, the control of the dc-link voltage can be acquired by regulating the current of the SC to the reference value i_{SC_ref} which is generated by the outer control loop.

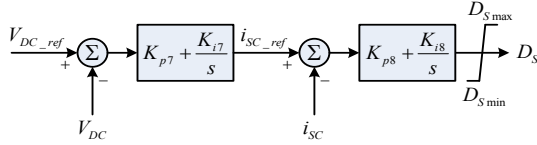


Fig. 9. Control block diagram of the bidirectional dc/dc converter.

IV. EIGENVALUE AND ROOT-LOCI ANALYSIS

A. System Eigenvalues

Table I lists the eigenvalues of the studied hybrid wave and PV system under the selected operating point, where the solar irradiance and the wave force are set at their highest values of 1000 W/m² and 0.9 MN, respectively. Although such the strongest conditions on solar irradiance and wave force do not always occur at the same time, it is worth examining the system eigenvalues under a most severe power-flow operating condition.

TABLE I. EIGENVALUES (rad/s) OF THE STUDIED SYSTEM UNDER THE SOLAR IRRADIANCE OF 1000 W/m² AND THE WAVE FORCE OF 0.9 MN

Mode No.	Eigenvalues	Mode No.	Eigenvalues
Λ_{1-2}	$-118.8020 \pm j24.7874$	Λ_{15-16}	$-0.22647; -1337.4160$
Λ_{3-4}	$-160.5717 \pm j4988129.7394$	Λ_{17-18}	$-204.3407; -497.0582$
Λ_{5-6}	$-160.6133 \pm j4987450.1423$	Λ_{19-20}	$-0.7989; -1.5997$
Λ_{7-8}	$-687.5884 \pm j299.0561$	Λ_{21-22}	$-693.6852 \pm j1232.9736$
Λ_{9-10}	$-493.8432 \pm j232.0693$	Λ_{23}	-3621.7926
Λ_{11-12}	$-9.7558; -9.6453$	Λ_{24-25}	$-0.1518; -0.2000$
Λ_{13-14}	$-0.3504; -1.2751$	Λ_{26-27}	$-114.6574; -20372.6950$

There are 27 eigenvalues of the studied system listed in Table I. The eigenvalues Λ_1 - Λ_{14} relate to the control modes of the VSI and the modes of the electrical interactions among ac side of the VSI. The eigenvalues Λ_{15} - Λ_{20} refer to the modes of the WPGS and the control modes of the VSC. The eigenvalues Λ_{21-22} and Λ_{23} are associated with the mode of the dc/dc boost converter and the dc link, respectively. The eigenvalues Λ_{24} - Λ_{27} relate to the modes of the SC and the bidirectional dc/dc converter. It is clearly seen that all the eigenvalues listed in Table I have negative real parts, which means that the studied system is stable under the specified operating point.

B. Root-Loci Analysis

Fig. 10 plots the root loci of the system eigenvalues when the solar irradiance G of the PV array is increased from 0 to 1000 W/m² and the wave force acting on the AWS of the WPGS is fixed at 0.9 MN. Only the root loci changing with the increase of the solar irradiance are plotted in Fig. 10. It is found that the eigenvalues Λ_{1-2} , Λ_{3-4} , Λ_{5-6} , and Λ_{21-22} move from the right-hand side to the left-hand side of the complex

plane when the solar irradiance increases, which indicates the damping improvement of these modes. On the other hand, the eigenvalues Λ_{7-8} and Λ_{9-10} move towards the imaginary of the complex plane and their oscillating frequencies get higher when the solar irradiance increases, which reveal that the damping ratios of these modes are decreased with the increase of the solar irradiance. It should be mentioned that the most noticeable movement is seen on the root loci of the eigenvalues Λ_{21-22} which relate to the mode of the dc/dc boost converter connecting the PV array. This mode locates near the imaginary axis when the solar irradiance equals to zero and moves rapidly to the left-hand side of the complex plane when the solar irradiance increases. Therefore, it can be concluded that the dynamic stability margin of the studied system is improved when the solar irradiance increases.

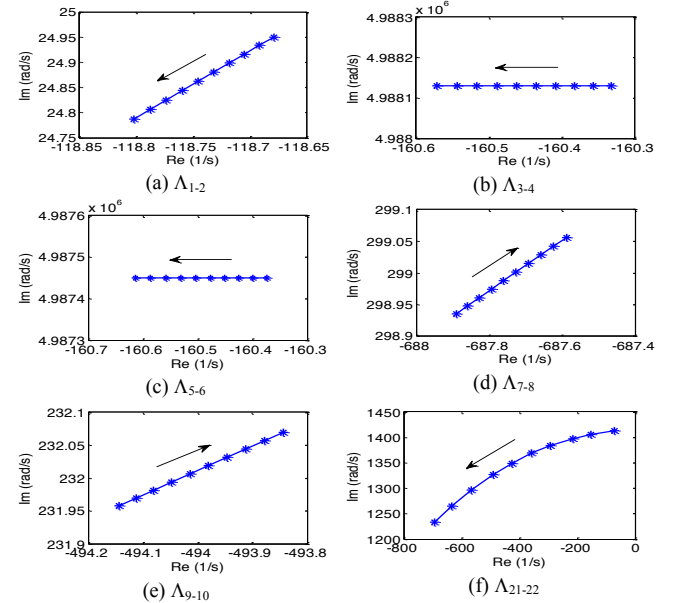


Fig. 10. Root loci of the studied system eigenvalues when the solar irradiance is increased from 0 to 1000 W/m².

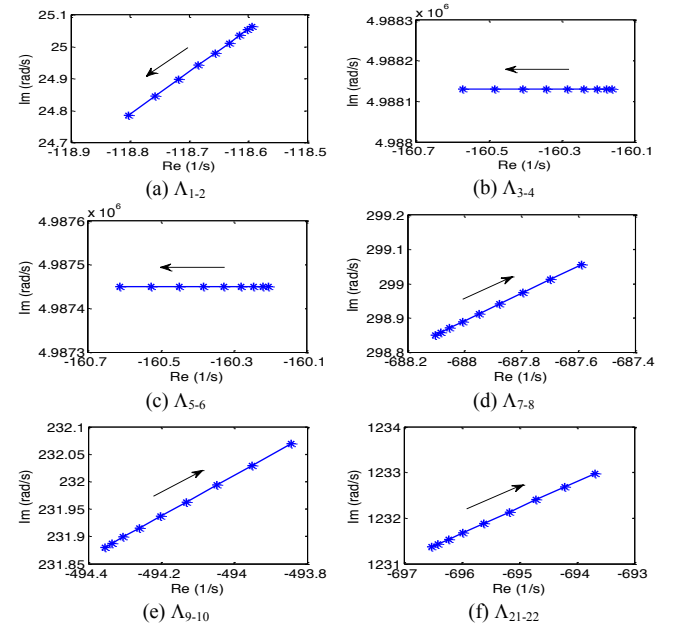


Fig. 11. Root loci of the studied system eigenvalues when wave force acting on the AWS of the WPGS is increased from 0.0 to 0.9 MN.

Fig. 11 depicts the root loci of the system eigenvalues when the wave force acting on the AWS of the WPGS is increased from 0.0 to 0.9 MN by keeping the solar irradiance at 1000 W/m². It is seen that the increase of the wave force from 0.0 to 0.9 MN makes the eigenvalues Λ_{1-2} , Λ_{3-4} , and Λ_{5-6} move leftward. Thus, the damping characteristics of these modes are improved with the increase of wave force. On the other hand, the eigenvalues Λ_{7-8} , Λ_{9-10} , and Λ_{21-22} move rightward and their oscillating frequencies are increased when the wave force increases, which means that the damping performance of these mode are deteriorated with the increase of the wave force. However, it can be clearly observed from Fig. 11 that all the root loci of the system eigenvalues are located on the left-hand side of the complex plane, which indicates that the studied system is quite stable under the wide-range variations of the wave force.

V. TIME-DOMAIN SIMULATIONS

A. Case 1: Variations of Wave Force

In this part, the wave force acting on the AWS of the WPGS is subject to the variations as depicted in Fig. 12(a) while the solar irradiance is assumed to be constant at 200 W/m². Initially, the peak amplitude and the period of the wave force are 0.7 MN and 12 s, respectively. Thereafter, the peak amplitude of wave force drops to 0.4 MN at $t = 40$ s and steeply increases to 0.9 MN at $t = 80$ s.

Figs. 12(b)-(f) show the dynamic responses of the studied system under the variations of the wave force. Since the solar irradiance is constant, the output power of the PV array, as plotted in Fig. 12(b), is a constant at around 8.83 kW, which is the maximum power of the PV array corresponding to the solar irradiance of 200 W/m². The speed of the AWS and instantaneous output power of the LPMG, as shown in Figs. 12(c)-(d), are continuously varied with time due to the variations of the wave force. The frequency of the speed response is the same as the frequency of the wave force while the frequency of the output power of the LPMG is twice the frequency of the wave force. The output power of the LPMG is reduced significantly when the peak amplitude of the wave force drops to 0.4 MN at $t = 40$ s and it is considerably increased when the peak amplitude of the wave force steps to 0.9 MN at $t = 80$ s. Figs. 12(e)-(g) depict the comparative responses of some other quantities of the studied system with and without the SC such as the active power fed to the distribution power grid, the voltage of the PCC, and the dc-link voltage. It can be clearly observed from these responses that the power fluctuations due to the variations of the wave can be effectively suppressed from transferring to the power grid and the dc-link voltage can be kept almost constant at its rated value when the studied system is equipped with the SC. In this case the power fluctuations have been controlled by the SC as illustrated in Fig. 12(h). On the other hand, when the studied system is without the SC, the power fluctuations due to the variations of the wave are reversed in the power fed to the power grid although the dc-link voltage can be maintained almost stable at its rated value. It can be concluded from the

simulation results that the SC combined with the proposed control scheme can effectively improve the performance of the studied system under the variations of the wave force acting on the AWS of the WPGS.

B. Case 2: Variations of Solar Irradiance

In this part, the solar irradiance at the PV array is subject to the variations as shown in Fig. 13(a) whereas wave force is kept at the peak amplitude of 0.2 MN and the period of 12 s. The solar irradiance is assumed to be increased from the initial value of 200 W/m² to the maximum level of 1000 W/m² at $t = 50$ s and gradually reduce back to 200 W/m² at $t = 200$ s. The variations of the solar irradiance are also assumed to contain the high-frequency fluctuations due to the fast changing of the local meteorological conditions.

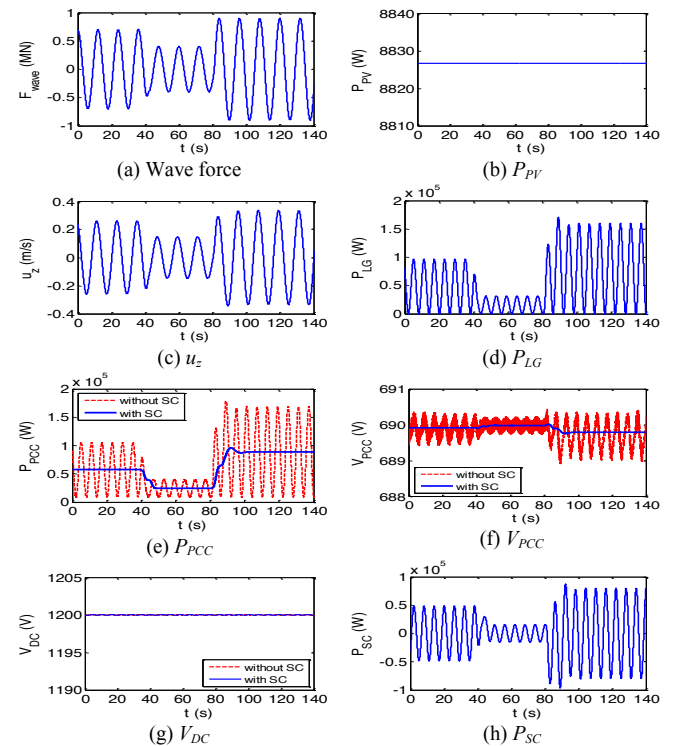


Fig. 12. Dynamic responses of the studied system under the variations of the wave force acting on the AWS of the WPGS.

Figs. 13(b) and (c) plot the dynamic responses of the output powers of the PV array and the LPMG, respectively. It is clearly seen in Fig. 13(b) that the output power of the PV array changes corresponding with the increase and decrease of the solar irradiance and also reflects the high-frequency fluctuations of the solar irradiance. It is also seen in Fig. 13(c) that the output power of the LPMG is not affected by the variations of the solar irradiance and its peak value is just about 8 kW since the peak amplitude of the wave force is relative small.

Figs. 13(d)-(e) show the comparative responses of the active power fed to the power grid and the dc-link voltage of the studied system with and without SC. It is clearly observed that when the studied system is equipped with the SC, the active power fed to the power grid is relatively smooth and the

dc-link voltage can be maintained at its rated value. The high-frequency power fluctuations generated by the PV array have been absorbed by the SC as depicted in Fig. 13(f). On the other hand, the active power fed to the power grid is considerably fluctuated when the SC is out of service, although the dc-link voltage can be maintained at its rated value.

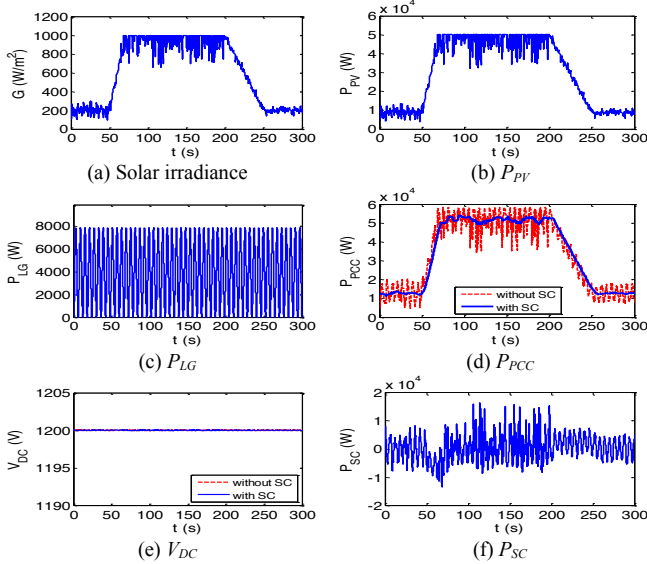


Fig. 13. Dynamic responses of the studied system under the variations of the solar irradiance.

C. Case 3: Effect of the Size of the Employed Supercapacitor

In this part, the effect of the size of the employed SC on the performance of the studied system is examined. Three different SCs with the power ratings of 30 kW, 60 kW, and 95 kW, are in turns employed for the studied system. It is also assumed that the variations of the wave force and the solar irradiance in the previous cases, which are shown in Fig. 12(a) and 13(a), respectively, are simultaneously applied to the studied system during the simulations. Fig. 14 depicts the comparative dynamic responses of the active power fed to the distribution power grid for the three different power ratings of the employed SC. It is clearly seen from the plots shown in Fig. 14 that when the size of the employed SC is increased, the active power fed to the distribution power grid is more smoothed, which demonstrates the further improvement in the performance of the studied system if the larger SC is employed.

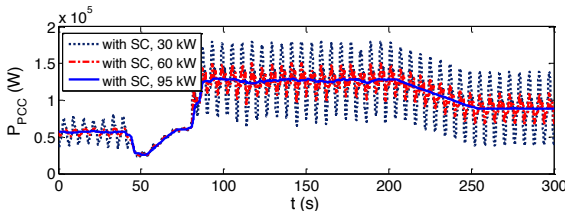


Fig. 14. Comparative dynamic responses of the active power fed to the distribution power grid for different power ratings of the employed SC.

VI. CONCLUSION

In this paper, the dynamic stability analysis results of a hybrid wave and PV system integrated into a distribution

power grid have been presented. An SC-based energy-storage system has been employed to support for smoothing out the power fluctuations. A control scheme has been proposed aiming to suppress the power fluctuations from feeding to the distribution power grid and maintain stable operation of the studied system while achieving the maximum power extractions from the PV array and the wave power-generation system. Both modal analysis and time-domain simulations of the studied system have been performed to examine the dynamic performance of the studied system under various operating conditions. It can be concluded from the simulation results that the proposed control scheme has the ability to maintain stable operation of the studied system under various operating conditions while extracting the maximum power from both the renewable-energy sources. It can also be concluded from the simulation results that the SC combined with the proposed control scheme can effectively smooth out the power fluctuations of the studied hybrid wave and PV system.

VII. APPENDIX

A. Sizing of the Employed Supercapacitor

The sizing of the SC used for smoothing power fluctuations was presented in several literatures [25], [35], [49]. In order to compensate the power fluctuations from the WPGS and the PV array, the SC will continuously exchange with the dc link a power quote, $P_{SC}(t)$, which is equal to the difference between the power generated by both the renewable sources and the power fed to distribution power grid. It should be noticed that when performing the sizing of the SC, the power profiles, $P_{LG}(t)$ and $P_{PV}(t)$, of the WPGS and the PV array must be given in advance and the sum of their average is taken as the power fed to the distribution power grid. Hence, the size of the SC, in terms of power and energy, can be determined by using the following equations:

$$P_{SC}(t) = [P_{LG}(t) + P_{PV}(t)] - [P_{LG,avg}(t) + P_{PV,avg}(t)] \quad (25)$$

$$E_{SC}(t) = \int_0^t P_{SC}(t) dt \quad (26)$$

where $P_{LG,avg}(t)$ and $P_{PV,avg}(t)$ are the average profiles of $P_{LG}(t)$ and $P_{PV}(t)$, respectively. The maximum values calculated by (25) and (26) can serve as the power rating and the energy rating of the SC, respectively. In this paper, it is assumed that $P_{LG}(t)$ and $P_{PV}(t)$ as given in Figs. 12(d) and 13(b) are the typical power profiles of the WPGS and the PV array. Based on these power profiles, the calculations using (25) and (26) result in the power and energy ratings of the SC are 95 kW and 0.5 kWh, respectively.

B. Employed System Parameters

The complete employed parameters of the studied system are listed in Table II below.

TABLE II. EMPLOYED SYSTEM PARAMETERS

160-kW AWS-based WPGS	
1) AWS [18]:	$K_D = 1.004 \times 10^6$ Ns/m, $K_S = 0.56$ MN/m, $m_t = 0.6$ Mkg,
	$F_{wave} = 0.9$ MN, $T_{wave} = 12$ s

2) LPMG [18]: $R_{LG} = 0.05 \Omega$, $L_{dLG} = L_{qLG} = L_{LG} = 31 \text{ mH}$, $\psi_{PM} = 23 \text{ Wb}$, $\tau_p = 0.05 \text{ ms}$
50-kW PV array and dc/dc boost converter
1) PV module (SUNPOWER SPR-305-WHT-D) [48]: $P_{mp} = 305.2 \text{ W}$, $V_{mp} = 54.7 \text{ V}$, $I_{mp} = 5.58 \text{ A}$, $N_s = 96 \text{ cells}$, $V_{oc,n} = 64.2 \text{ V}$, $I_{sc,n} = 5.96 \text{ A}$, $R_s = 0.037998 \Omega$, $R_p = 993.51 \Omega$
2) PV array: $N_{ms} = 11$, $N_{mp} = 15$, $R_{sa} = (N_{ms}/N_{mp}) \times R_s$, $R_{pa} = (N_{ms}/N_{mp}) \times R_p$, $A = 1.3$, $q = 1.6022 \times 10^{-19} \text{ C}$, $k = 1.3806 \times 10^{-23} \text{ J/K}$, $k_f = 0.003516 \text{ A/K}$, $E_g = 1.12 \text{ eV}$
3) dc/dc boost converter: $C_{pr} = 100 \mu\text{F}$, $R_p = 0.005 \Omega$, $L_p = 5 \text{ mH}$
DC link and AC grid
$V_{DC} = 1200 \text{ V}$, $C_{DC} = 0.4 \text{ F}$ $R_f = 0.002 \Omega$, $L_f = 205 \mu\text{H}$, $C_f = 84 \mu\text{F}$, $R_{TL} = 0.001 \Omega$, $L_{TL} = 50 \mu\text{H}$
SC and bidirectional dc/dc converter
1) SC model: $C_{SC} = 8.7 \text{ F}$, $R_{sSC} = 0.16 \Omega$, $R_{pSC} = 4.2 \times 10^3 \Omega$, 2) Bidirectional dc/dc converter: $R_s = 0.001 \Omega$, $L_s = 1.0 \text{ mH}$
Controllers
$K_{p1} = 10$, $K_{i1} = 8 \text{ s}$, $K_{p2} = 5$, $K_{i2} = 8 \text{ s}$, $K_{p3} = 0.2$, $K_{i3} = 100 \text{ s}$, $K_{p4} = K_{p6} = 0.205$, $K_{i4} = K_{i6} = 2 \text{ s}$, $K_{p5} = 0.5$, $K_{i5} = 200 \text{ s}$, $K_{p7} = 5$, $K_{i7} = 50 \text{ s}$, $K_{p8} = 0.0017$, $K_{i8} = 0.195 \text{ s}$

VIII. REFERENCES

- [1] M. Sandhu and T. Thakur, "Issues, challenges, causes, impacts and utilization of renewable energy sources - Grid integration," *Int. J. Engineering Research and Applications*, vol. 4, no. 3, pp. 636-643, Mar. 2014.
- [2] S.-K. Kim, J.-H. Jeon, C.-H. Cho, J.-B. Ahn, and S.-H. Kwon, "Dynamic modeling and control of a grid-connected hybrid generation system with versatile power transfer," *IEEE Trans. Industrial Electronics*, vol. 55, no. 4, pp. 1677-1688, Apr. 2008.
- [3] X. Liu, P. Wang, and P. C. Loh, "A hybrid ac/dc microgrid and its coordination control," *IEEE Trans. Smart Grid*, vol. 2, no. 2, pp. 278-286, Jun. 2011.
- [4] M. M. R. Singaravel and S. A. Daniel, "MPPT with single dc-dc converter and inverter for grid-connected hybrid wind-driven PMSG-PV system," *IEEE Trans. Industrial Electronics*, vol. 62, no. 8, pp. 4849-4857, Aug. 2015.
- [5] Y. J. Reddy, Y. V. P. Kumar, K. P. Raju, and A. Ramsesh, "Retrofitted hybrid power system design with renewable energy sources for buildings," *IEEE Trans. Smart Grid*, vol. 3, no. 4, pp. 2174-2187, Dec. 2012.
- [6] C. Wang and M. H. Nehrir, "Power management of a stand-alone wind/photovoltaic/fuel cell energy system," *IEEE Trans. Energy Conversion*, vol. 23, no. 3, pp. 957-967, Sep. 2008.
- [7] L. N. Khanh, J.-J. Seo, Y.-S. Kim, and D.-J. Won, "Power-management strategies for a grid-connected PV-FC hybrid system," *IEEE Trans. Power Delivery*, vol. 25, no. 3, pp. 1874-1882, Jul. 2010.
- [8] P. Garcia, C. A. Garcia, L. M. Fernandez, F. Llorens, and F. Jurado, "ANFIS-based control of a grid-connected hybrid system integrating renewable energies, hydrogen and battery," *IEEE Trans. Industrial Informatics*, vol. 10, no. 2, pp. 1107-1117, May 2014.
- [9] B. Liu, F. Zhuo, Y. Zhu, and H. Yi, "System operation and energy management of a renewable energy-based dc micro-grid for high penetration depth application," *IEEE Trans. Smart Grid*, vol. 6, no. 3, pp. 1147-1155, May 2015.
- [10] D. Abbes, A. Martinez, and G. Champenois, "Eco-design optimization of an autonomous hybrid wind-photovoltaic system with battery storage," *IET Renewable Power Generation*, vol. 6, no. 5, pp. 358-371, Sep. 2012.
- [11] M. B. Shadmand and R. S. Balog, "Multi-objective optimization and design of photovoltaic-wind hybrid system for community smart dc microgrid," *IEEE Trans. Smart Grid*, vol. 5, no. 5, pp. 2635-2643, Sep. 2014.
- [12] X. Tang, W. Deng, and Z. Qi, "Investigation of the dynamic stability of microgrid," *IEEE Trans. Power Systems*, vol. 29, no. 2, pp. 698-706, Mar. 2014.
- [13] S. Mishra and D. Ramasubramanian, "Improving the small signal stability of a PV-DE-dynamic load-based microgrid using an auxiliary signal in the PV control loop," *IEEE Trans. Power Systems*, vol. 30, no. 1, pp. 166-176, Jan. 2015.
- [14] X. Li, D. Hui, and X. Lai, "Battery energy storage station (BESS)-based smoothing control of photovoltaic (PV) and wind power generation fluctuations," *IEEE Trans. Sustainable Energy*, vol. 4, no. 2, pp. 464-473, Apr. 2013.
- [15] S.-T. Kim, B.-K. Kang, S.-H. Bae, and J.-W. Park, "Application of SMES and grid code compliance to wind/photovoltaic generation system," *IEEE Trans. Applied Superconductivity*, vol. 23, no. 3, pp. 5000804, Jun. 2013.
- [16] J. Khan and U. Nasir, "Voltage stabilization of hybrid micro-grid using super capacitors," *J. Power and Energy Engineering*, vol. 3, no. 6, pp. 1-9, Jun. 2015.
- [17] S. Ceballos, J. Rea, I. Lopez, J. Pou, E. Robles, and D. L. O'Sullivan, "Efficiency optimization in low inertia Wells turbine-oscillating water column devices," *IEEE Trans. Energy Conversion*, vol. 28, no. 3, pp. 553-564, Sep. 2013.
- [18] F. Wu, X.-P. Zhang, P. Ju, and M. J. H. Sterling, "Optimal control for AWS-based wave energy conversion system," *IEEE Trans. Power Systems*, vol. 24, no. 4, pp. 1747-1755, Sep. 2009.
- [19] Z. Nie, X. Xiao, R. McMahon, P. Clifton, Y. Wu, and S. Shao, "Emulation and control methods for direct drive linear wave energy converters," *IEEE Trans. Industrial Informatics*, vol. 9, no. 2, pp. 790-798, May 2013.
- [20] L. Cappelli, F. Marignetti, G. Mattiazzo, E. Giorcelli, G. Bracco, S. Carbone, and C. Attiaianese, "Linear tubular permanent-magnet generators for the inertial sea wave energy converter," *IEEE Trans. Industry Applications*, vol. 50, no. 3, pp. 1817-1828, May/Jun. 2014.
- [21] J. Prudell, M. Stoddard, E. Amon, T. K. A. Brekken, and A. von Jouanne, "A permanent-magnet tubular linear generator for ocean wave energy conversion," *IEEE Trans. Industry Applications*, vol. 46, no. 6, pp. 2392-2400, Nov./Dec. 2010.
- [22] H. Polinder, M. E. C. Damen, and F. Gardner, "Linear PM generator system for wave energy conversion in the AWS," *IEEE Trans. Energy Conversion*, vol. 19, no. 3, pp. 583-589, Sep. 2004.
- [23] F. Wu, X.-P. Zhang, P. Ju, and M. J. H. Sterling, "Modeling and control of AWS-based wave energy conversion system integrated into power grid," *IEEE Trans. Power Systems*, vol. 23, no. 3, pp. 1196-1204, Aug. 2008.
- [24] F. Wu, P. Ju, X.-P. Zhang, C. Qin, G. J. Peng, H. Huang, and J. Fang, "Modeling, control strategy, and power conditioning for direct-drive wave energy conversion to operate with power grid," *Proc. IEEE*, vol. 101, no. 4, pp. 925-941, Apr. 2013.
- [25] G. Brando, A. Dannier, A. D. Pizzo, L. P. D. Noia, and C. Pisani, "Grid connection of wave energy converter in heaving mode operation by supercapacitor storage technology," *IET Renewable Power Generation*, vol. 10, no. 1, pp. 88-97, Jan. 2016.
- [26] M. Alberdi, M. Amundarain, A. J. Garrido, I. Garrido, O. Casquero, and M. D. la Sen, "Complementary control of oscillating water column-based wave energy conversion plants to improve the instantaneous power output," *IEEE Trans. Energy Conversion*, vol. 26, no. 4, pp. 1021-1032, Dec. 2011.
- [27] A. J. Garrido, I. Garrido, M. Amundarain, M. Alberdi, and M. D. la Sen, "Sliding-mode control of wave power generation plants," *IEEE Trans. Industry Applications*, vol. 48, no. 6, pp. 2372-2381, Nov./Dec. 2012.
- [28] G. Bacelli, P. Balitsky, and J. V. Ringwood, "Coordinated control of arrays of wave energy devices-Benefits over independent control," *IEEE Trans. Sustainable Energy*, vol. 4, no. 4, pp. 1091-1099, Oct. 2013.
- [29] M. I. Marei, M. Mokhtar, and A. A. El-Sattar, "MPPT strategy based on speed control for AWS-based wave energy conversion system," *Renewable Energy*, vol. 83, pp. 305-317, Nov. 2015.
- [30] S.-Y. Lu, L. Wang, T.-M. Lo, and A. V. Prokhorov, "Integration of wind power and wave power generation systems using a dc microgrid," *IEEE Trans. Industry Applications*, vol. 51, no. 4, pp. 2753-2761, Jul./Aug. 2015.
- [31] T. Ahmed, "Electrical technologies for grid integration of ocean wave power into the UK national grid," *J. Power Electronics*, vol. 10, no. 3, pp. 320-327, May 2010.
- [32] N. H. Samrat, N. B. Ahmad, I. A. Choudhury, and Z. B. Taha, "Modeling, control, and simulation of battery storage photovoltaic-wave energy hybrid renewable power generation systems for island electrification in Malaysia," *The Scientific World Journal*, pp. 1-21, Apr. 2014.
- [33] G. Wang, M. Ciobotaru, and V. G. Agelidis, "Power smoothing of large solar PV plant using hybrid energy storage," *IEEE Trans. Sustainable Energy*, vol. 5, no. 3, pp. 834-842, Jul. 2014.
- [34] Z. Nie, X. Xiao, Q. Kang, R. Aggarwal, H. Zhang, and W. Yuan, "SMES-battery energy storage system for conditioning outputs from

- direct drive linear wave energy converters,” *IEEE Trans. Applied Superconductivity*, vol. 23, no. 3, pp. 5000705, Jun. 2013.
- [35] Z. Zhou, M. Benbouzid, J. F. Charpentier, F. Scuiller, and T. Tang, “A review of energy storage technologies for marine current energy systems,” *Renewable and Sustainable Energy Reviews*, vol. 18, pp. 390-400, Feb. 2013.
- [36] S. Mallika and R. S. Kumar, “Review on ultracapacitor-battery interface for energy management system,” *Int. J. Engineering and Technology*, vol. 3, no. 1, pp. 37-43, Feb. 2011.
- [37] M. H. Ali, B. Wu, and R. A. Dougal, “An overview of SMES applications in power and energy systems,” *IEEE Trans. Sustainable Energy*, vol. 1, no. 1, pp. 38-47, Apr. 2010.
- [38] C. Hua, J. Lin, and C. Shen, “Implementation of a DSP-controlled photovoltaic system with peak power tracking,” *IEEE Trans. Industrial Electronics*, vol. 45, no. 1, pp. 99-107, Feb. 1998.
- [39] K. H. Hussein, I. Muta, T. Hoshino, and M. Osakada, “Maximum photovoltaic power tracking: an algorithm for rapidly changing atmospheric conditions,” *IEE Proc.-Generation, Transmission and Distribution*, vol. 142, no. 1, pp. 59-64, Jan. 1995.
- [40] M. G. Villalva, J. R. Gazoli, and E. R. Filho, “Modeling and circuit-based simulation of photovoltaic arrays,” in *Proc. 2009 Brazilian Power Electronics Conf.*, 2009, pp. 1244-1254.
- [41] M. G. Villalva, J. R. Gazoli, and E. R. Filho, “Comprehensive approach to modeling and simulation of photovoltaic arrays,” *IEEE Trans. Power Electronics*, vol. 24, no. 5, pp. 1198-1208, May 2009.
- [42] A. Chikh and A. Chandra, “An optimal maximum power point tracking algorithm for PV systems with climatic parameters estimation,” *IEEE Trans. Sustainable Energy*, vol. 6, no. 2, pp. 644-652, Apr. 2015.
- [43] J. Mahdavi, A. Emadi, and H. A. Toliyat, “Application of state space averaging method to sliding mode control of PWM DC/DC converters,” in *Proc. 32nd IEEE Industry Applications Society Annual Meeting*, 1997, pp. 820-827.
- [44] H. Abdel-Gawad and V. K. Sood, “Small-signal analysis of boost converter, including parasitics, operating in CCM,” in *Proc. 2014 6th IEEE Power India Int. Conf.*, 2014, pp. 1-5.
- [45] A. S. Samosir and A. H. M. Yatim, “Implementation of dynamic evolution control of bidirectional dc-dc converter for interfacing ultracapacitor energy storage to fuel-cell system,” *IEEE Trans. Industrial Electronics*, vol. 57, no. 10, pp. 3468-3473, Oct. 2010.
- [46] Z. Shi, F. Auger, E. Schaeffer, P. Guillemet, and L. Loron, “Interconnected observers for online supercapacitor ageing monitoring,” in *Proc. 39th Annual Conf. IEEE Industrial Electronics Society (IECON 2013)*, pp. 6746-6751.
- [47] H.-L. Do, “Nonisolated bidirectional zero-voltage-switching dc-dc converter,” *IEEE Trans. Power Electronics*, vol. 26, no. 9, pp. 2563-2569, Sep. 2011.
- [48] J. Hossain and A. Mahmud, *Renewable Energy Integration: Challenges and Solutions*. Singapore: Springer, 2014.
- [49] J. Aubry, P. Bydlowski, B. Multon, H. B. Ahmed, and B. Borgarino, “Energy storage system sizing for smoothing power generation of direct wave energy converters,” in *Proc. 3th Int. Conf. Ocean Energy*, 2010, pp. 1-7.